Article

Black-Si as photoelectrode

Denver P. Linklater[1,2,3]*, Fatima Haydous[4,5], Cheng Xi[4], Daniele Pergolesi[4], Jingwen Hu[3], Elena P. Ivanova[1], Saulius Juodkazis[3,6], Thomas Lippert[4], Jurga Juodkazytė[7]

1 School of Science, RMIT University, Melbourne, VIC 3000, Australia
2 Melbourne Centre for Nanofabrication, ANFF, 151 Wellington Road, Clayton, VIC 3168, Australia
3 Optical Sciences Centre and ARC Training Centre in Surface Engineering for Advanced Materials (SEAM), School of Science, Swinburne University of Technology, Hawthorn, VIC 3122, Australia
4 Laboratory for Multiscale Materials Experiments, Paul Scherrer Institut, CH-5232 Villigen PSI, Switzerland
6 Tokyo Tech World Research Hub Initiative (WRHI), School of Materials and Chemical Technology, Tokyo Institute of Technology, 2-12-1, Ookayama, Meguro-ku, Tokyo 152-8550, Japan
7 Center for Physical Sciences and Technology, Saulėtekio ave. 3, LT-10257 Vilnius, Lithuania
* Correspondence: (D.L.) denver.linklater@rmit.edu.au; (T. L.) Thomas.Lippert@psi.ch; (J. J.) jurga.juodkazyte@ftmc.lt
† Current address: [5] KTH Royal Institute of Technology, Division of Applied Physical Chemistry, Teknikringen 30, SE-114 28, Stockholm, Sweden

Received: date; Accepted: date; Published: date

Abstract: The fabrication and characterisation of photo-anodes based on black-Si (b-Si) is presented using a photo-electrochemical cell in NaOH solution. Black-Si was fabricated by maskless dry plasma etching and was conformally coated by tens-of-nm of TiO_2 using atomic layer deposition (ALD) with a top layer of CoO_x cocatalyst deposited by pulsed laser deposition (PLD). Low reflectivity $R < 5\%$ of Black-Si over the entire visible and near-IR ($\lambda < 2$ μm) spectral range is favorable in better absorption of light while an increased surface area facilities larger current densities. Photoelectrochemical performance of the heterostructured photoanode is discussed in terms of n-n junction between b-Si and TiO_2.

Keywords: black Si; antireflection; photo-anode; water splitting

1. Introduction

Nanotextured silicon - Black-Si [1] - has a range of useful properties: it acts as an antireflection surface over the vis-IR spectral range, has bactericidal activity against gram positive and negative bacteria [2] (Fig. 1(a)), can rupture soft membranes of red blood cells [3], can act as a field emitter electrode [4], can be rendered into a hydrophobic surface, substrates for surface enhanced Raman sensors/spectroscopy (SERS) [5] and it is used for solar cells [6,7]. Recently, optical binding/trapping of Black-Si was demonstrated at very high laser powers when nonlinear optical effects inside trapped material can be induced [8]. High thermal conductivity of Black-Si due to its crystalline nature is a useful property in heat dissipation also helped by the larger surface area of Black-Si. This wide range of applications are enabled by the specific physico-chemical properties of the nanostructured silicon surface. Black-Si surface topography presents with a random array of high aspect ratio spikes that can efficiently trap light (enhance absorption and reflection since reflection is suppressed), due to gradual refractive index change.

There is increasing interest to use black-Si as a photoelectrode in photelectrochemical (PEC) splitting of water as both a photoanode and photocathode. Nanoporous p-type b-Si with a hybrid organic/inorganic interfacial architecture, consisting of organic molecular monolayer beneath ALD-deposited TiO_2 modified with Pt nanoparticles (NPs), was recently studied as a photocathode [9]. The critical importance of careful consideration of semiconductor junction engineering was pinpointed. Yang et al. (2019) [10], introduced a dual protection layer strategy where the first layer of TiO_2 was ALD deposited on p-type nanoporous Black-Si, while the second layer was deposited on top

Preprints (www.preprints.org) | NOT PEER-REVIEWED | Posted: 10 April 2020 doi:10.20944/preprints202004.0169.v1

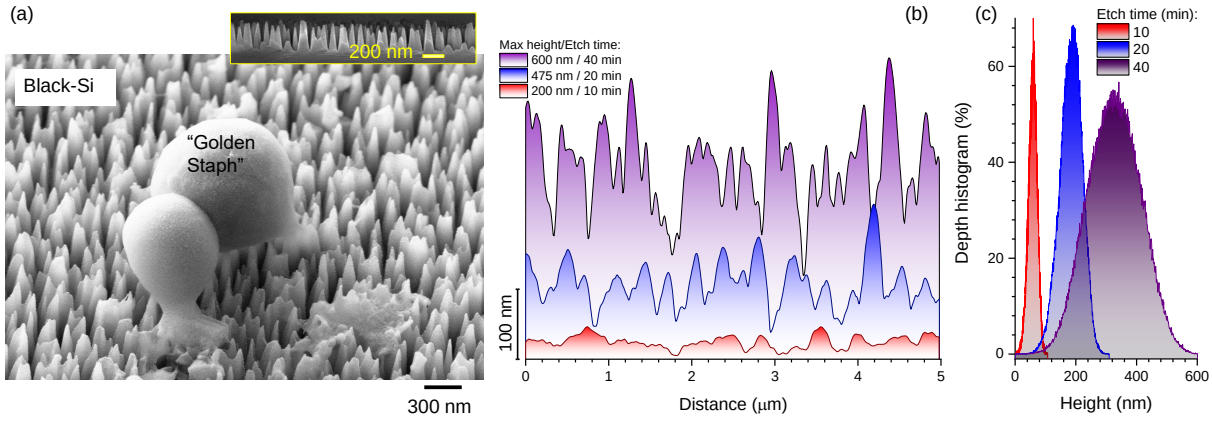

Figure 1. Mechanically bactericidal surface of Black-Si. (a) SEM image of a Gram-positive *Staphylococcus aureus* "Golden Staph" cell ruptured on b-Si. Inset shows SEM side-view image of Black-Si prepared by typical 15 min dry plasma etching with SF_6 and O_2 gases. (b) Height profiles of AFM cross sections for different plasma dry etching times of 10, 20 and 40 min. (c) Depth histogram: a depth (height) pixel distribution in the AFM image of Black-Si etched for different times (see Appendix for the bearing ratios and statistical analysis).

of the hydrogen evolution reaction (HER) cocatalyst. Significant improvement in the durability of Black-Si photocathodes in both acid and alkaline medium was demonstrated. Contrary to these results, Oh et al., (2019) [11] reported that transition metal NPs electrodeposited directly on n-type Black-Si surface can stabilize photoanodes without the need for a protection layer. However, the role of protective layer in their study was, in fact, played by thermally grown SiO_x. Recently, Black-Si demonstrated enhanced photoelectrochemical efficiency and stability using a conformal TiO_2 film on a nanoporous n-type silicon photoanode [12]. This b$-$Si/TiO_2/$Co(OH)_2$ nanostructured photoelectrode produced a saturated photocurrent density of 32.3 mA.cm^{-2} at an external potential of 1.48 V versus reference reference electrode (RHE) in 1 M NaOH electrolyte under 1 Sun illumination. The authors demonstrated that amorphous ALD TiO_2 layer was able to passivate defective surface sites, increase the efficiency of electron-hole separation as well as lifetime of minority charge carriers in n-type Black-Si PEC photoelectrodes.

Here, Black-Si surfaces were assessed for their photoelectrochemical (PEC) performance by exploring the influence of surface spike topography (height/pitch) and TiO_2 film thickness. A layer of CoO_x as oxygen evolution reaction (OER) cocatalyst was explored to enhance the photo-current output.

2. Experimental

Fabrication of photo-anodes. Black-Si was fabricated using n-type As-doped 100 mm diameter silicon wafers with specific resistivity of 0.005 Ω.cm and processed with a Samco RIE101iPH inductively coupled plasma (ICP) assisted reactive ion etching (RIE) tool. Silicon surfaces were initially cleaned with isopropanol and then dried under nitrogen gas flow to remove contaminants. Silicon wafers were then etched according to the following recipe: the etchant gases were SF_6/O_2 with respective flow rates of 35/45 sccm. Process pressure was 1 Pa, ICP power of 150 W, and RIE bias power of 15 W. Etching time was varied between 10 and 40 min to produce high aspect ratio nanopillars of differing heights (Fig. 1). During the etch process, the spontaneous passivation mask was not efficiently removed during alternating rounds of etching and deposition, therefore a simple 10 wt% sulphuric acid solution and sonication for 10 min was used to remove the contaminative mask. Figure 1 shows typical surface pattern measured by scanning electron microscopy (SEM) and height profiles obtained by atomic force microscopy (AFM).

Preprints (www.preprints.org) | NOT PEER-REVIEWED | Posted: 10 April 2020 doi:10.20944/preprints202004.0169.v1

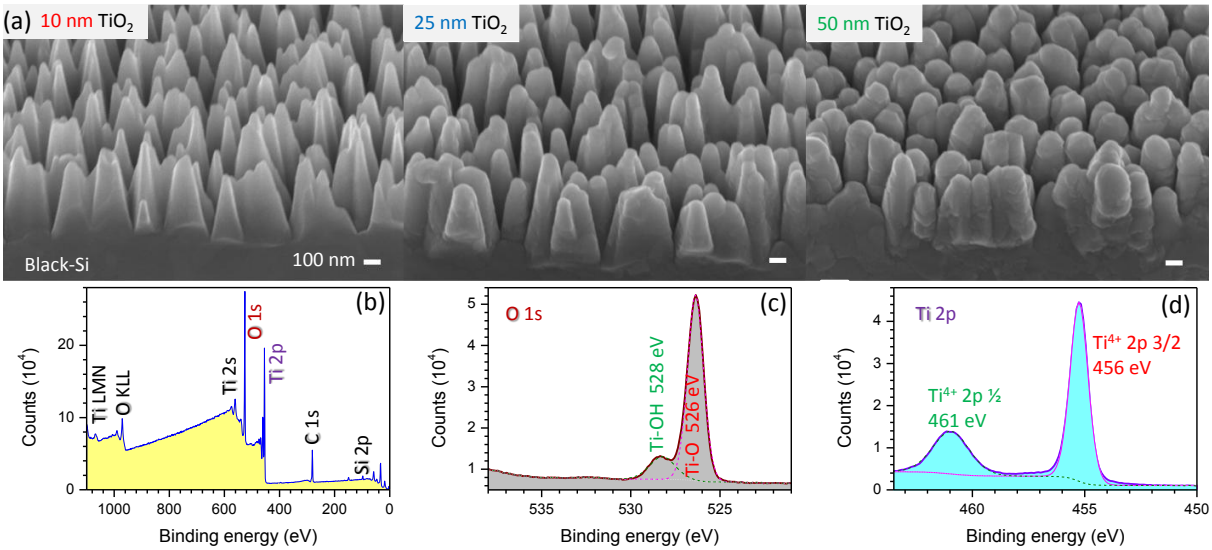

Figure 2. Surface characterisation of Black-Si photoelectrodes. (a) Side-view SEM images of Black-Si coated with different thickness of TiO_2 by atomic layer deposition (ALD). Scale bars 100 nm. Black-Si was etched for 40 min. (b-d) XPS surface analysis for wide and narrow spectral windows at O1s and Ti2p bands from sample coated with 25 nm of TiO_2.

TiO_2 thin films of 10, 25 or 50 nm were deposited using atomic layer deposition (ALD) (Cambridge Nanotech ALD Fiji F200 & Savannah s100). Black-Si samples were used for the ALD coating without removal of native oxide. Figure 2 shows SEM images and X-ray photo-electron spectroscopy (XPS) characterisaiton of the surfaces after TiO_2 deposition. A cobalt oxide CoO_x cocatalyst layer was deposited using pulsed laser deposition (PLD) setup based on a 248 nm wavelength KrF eximer laser [13]; PLD is a practical method to deposit materials from targets with complex composition at fast deposition rate. Surface morphology was inspected by SEM.

PEC Measurements. PEC measurements were performed in a three-electrode configuration in 0.5 M NaOH (pH 13.0) aqueous solution. The b-Si photoelectrode was used as the working electrode. Silver paste was applied for the electrical connection between the sample and the clamped wire; an epoxy resin covered the contact and insulated it from the electrolyte. Epoxy resin was also used to insulate the back side and the edges of the b-Si sample to avoid electrical short-circuit with only the front side of the sample exposed to the electrolyte and light. A coiled Pt wire and Ag/AgCl were used as the counter and reference electrodes, respectively. To simplify the display of the working electrode potential, the potential versus reference hydrogen electrode (RHE), obtained according to the relation E(vs RHE) = E(vs Ag/AgCl) + 0.197 + 0.059pH, has been adopted throughout this article. A Solartron 1286 electrochemical interface was used to carry out the voltage scan and current collection. Potentiodynamic measurements with a scan rate of 10 mV/s in the potential window of 0.5 - 1.7 V RHE were performed to investigate the PEC performance of b-Si-TiO_2 multiphases. The chopped dark-light current densities were normalized according to the illuminated area. The light source was a 150 W Xe lamp equipped with an AM 1.5G filter (100 mW/cm^2, Newport 66477-150XF-R1) calibrated with a photodetector (Gentec-EO).

3. Results and Discussion

Black-Si has antireflective properties across the entire visible spectrum range [14,15] with a reflectivity of only a few percent $R < 5\%$ after 30 min of plasma etching. Since Si can be either n-/p-type electrode it was interesting to explore application of Black-Si as a photo-electrode with more efficient light absorption. Also, an increase of surface area of Black-Si due to its nanotexture [16] is another advantage for a large current operation of photo-electrochemical cell. Complex pathways of (photo)electrochemical modification of Si are possible in acidic solutions due to the different valence

Preprints (www.preprints.org) | NOT PEER-REVIEWED | Posted: 10 April 2020 doi:10.20944/preprints202004.0169.v1

states of Si [17]. In basic solutions, Si is usually stable at room temperature [18], hence, is promising as an electrode. When metals or semiconductors are deposited over Black-Si surfaces, a light scattering pattern creates de-polarisation of light and the E-field component perpendicular to the electrode or catalyst surface could be formed and facilitate a charge (electron or hole) transport through the interface [19].

3.1. Black-Si with TiO_2: potentiostatic and potentiodynamic scans

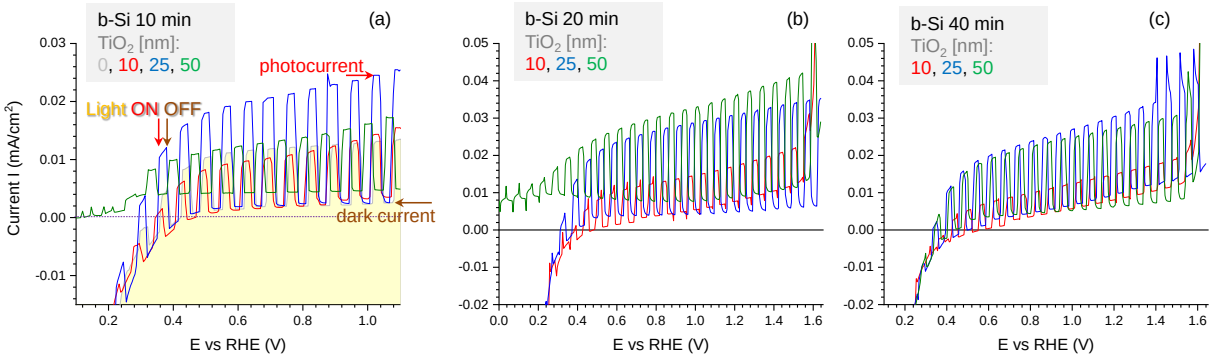

Figure 3. Potentiodynamic scans for the Black-Si photoanodes fabricated for 10, 20 and 40 min and coated with 10, 25, or 50 nm TiO_2, respectively in NaOH electrolyte under chopped light illumination; x,y-scales are different for a better presentation.

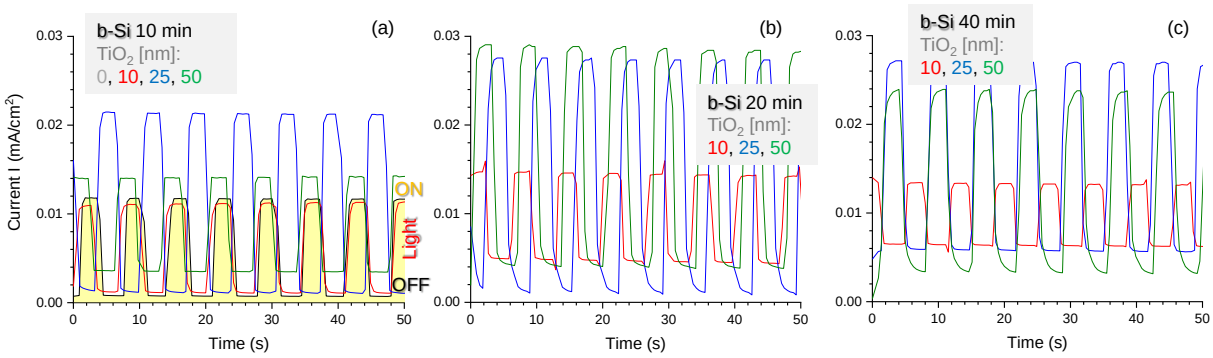

Figure 4. Potentiostatic scan at 1.23 V vs RHE for the Black-Si photoanodes fabricated for 10, 20 and 40 min and coated with 10, 25, or 50 nm TiO_2, respectively in NaOH electrolyte under chopped light illumination.

Potentiodynamic polarization curves recorded in the solution of 0.5 M NaOH under chopped illumination for b-Si electrodes fabricated using different etching times and coated with TiO_2 layers of different thickness are compared in Fig. 3. A slight increase in the magnitude of dark currents with increase in etching duration can be observed in Figs. 3(a-c). This can be attributed to the increase in electrochemically active surface area of the electrode with etching time, which is consistent with the height profiles of AFM cross-sections shown in Fig. 1(b). Another observation is that the deposition of TiO_2 on Black-Si leads to an increase in photoanodic current. This is especially obvious in the case of Black-Si samples with higher roughness, i.e., etched for 20 and 40 min. The most significant effect of TiO_2 on the photocurrent is observed when its thickness increases from 10 nm to 25 nm, whereas further thickening of the layer up to 50 nm was not efficient in terms of photoelectrochemical performance of the samples.

The same regularities can be seen in chronoamperograms run under chopped illumination at the stationary potential of 1.23 V (Fig. 4). The highest photocurrents (taken as difference between the current values in dark and under illumination) were observed in the case of Black-Si samples

Preprints (www.preprints.org) | NOT PEER-REVIEWED | Posted: 10 April 2020 doi:10.20944/preprints202004.0169.v1

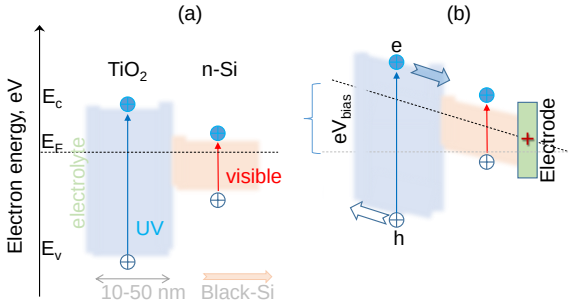

Figure 5. Band diagram of n-n junction between Si and TiO_2 without (a) and with (b) bias. Black-Si was made on n-type Si. Under positive bias, holes are drifting to the titania-solution interface while electrons are drawn into the electrode bulk. Bandgap of TiO_2 is 3.1 eV (400 nm) and 1.12 eV for Si. Under a white light (spectrally broad) illumination, e-h generation occurs at the both materials forming a TiO_2-Si n-n-junction. Arrows show e,h drift direction.

etched for 20 min with 25 nm thick TiO_2 layer (Fig. 4(b)), which means that such fabrication conditions ensure the most efficient generation, separation and transport of the charge carriers. To analyze these processes in more detail, energy band diagram of n-n junction between n-type Black-Si and n-type TiO_2 has been constructed and is shown in Fig. 5. These semiconductors form type-I, or straddling gap, heterojunction. In accordance with the their bandgap values, i.e. 3.1 eV for TiO_2 and 1.12 eV for Si, titania will absorb UV portion of incident light, while silicon will absorb longer wavelengths. In the case of a n-type photoanode immersed into electrolyte solution under illumination (white light), photogenerated holes should be drifting to semiconductor-electrolyte interface to participate in the oxidation of solution species (water molecules), whereas photoelectrons should be driven to the electrode bulk and towards counter electrode to take part in the reduction reaction. Due to upward band bending at the hetrojunction between the two n-type semiconductors, an energy barrier is formed for the transport of photo-generated electrons from the conduction band of TiO_2 to that of Si (Fig. 5(a) at no external bias conditions. The barrier for photoholes drifting from the valence band of Si to the valence band ofTiO_2 is even higher. Positive polarization of the electrode provides the energy required to overcome this barrier (Fig. 5(b)) and this is the reason why photocurrent increases with increase in electrode potential as can be seen in Fig. 3.

The surface area increase with etching time t can be evaluated from the height evolution of the Black-Si pyramids as $h(t)$ [15]. Side walls of pyramids has $\sim 6^\circ$ angle with the normal to the initial flat surface of Si. The surface area of b-Si can be estimated from a scaling argument by measuring the side-length $x(t)^2$ where x is measured from a side-view of b-Si cross section (inset in Fig. 1(a)). A linear evolution of the height was $h(t) \propto 4.5 \times h(15\text{ min})$. The x-length of cross-section after $t_1 = 15$ min etching was increasing $x(15\text{ min})/x(0\text{ min}) \approx 3.96$ times, hence the area increase was $x^2 \propto 15.7$ times. For longer etching times $x(h)^2 \propto \sqrt{h/h(t_1)}x(t_1)^2$, where $t_1 = 15$ min. After 45 nm etching, $h = 900$ nm tall pyramids of Black-Si are fromed [15] and the surface area was approximately 30 times larger as compared the initial flat surface of Si.

3.2. Black-Si with TiO_2 and CoO_x: potentiostatic and potentiodynamic scans

Semiconductor modification with oxygen/hydrogen evolution (OER/HER) cocatalysts is a common strategy to increase the efficiency of photoelectrochemical water splitting reactions [20]. In this study 150 nm thick layer of cobalt oxide CoO_x was deposited on b-Si fabricated for 20 min and coated with 10 nm TiO_2. The surface morphology of as-fabricated sample is shown in Fig. 6. Deposition of materials of 10-100 nm thickness over a nano-rough surface of b-Si by different methods (sputtering, e-beam or thermal evaporation) usually maintains high surface area and nano-roughness which decrease reflectivity and increase/maintains larger surface area. The presence of cobalt oxide crystallites on the surface of b-Si/TiO_2 spikes is clearly recognisable (Fig. 6). It is important to note

Preprints (www.preprints.org) | NOT PEER-REVIEWED | Posted: 10 April 2020 doi:10.20944/preprints202004.0169.v1

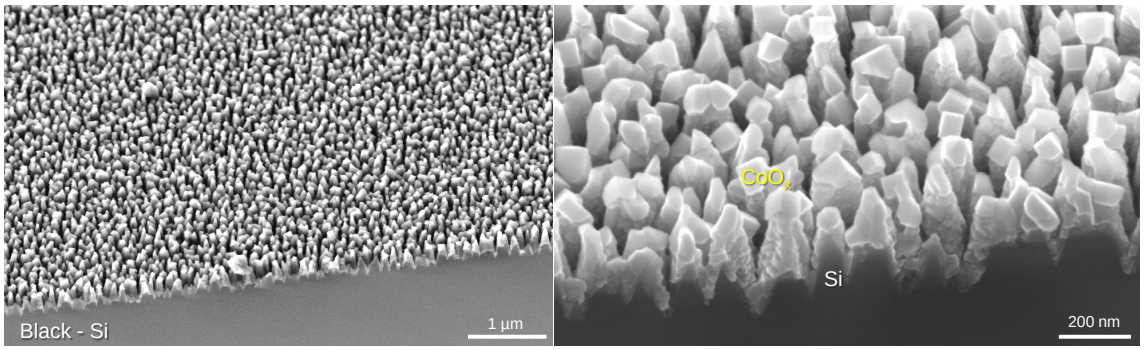

Figure 6. SEM images of as-fabricated Black-Si photoanodes etched for 20 min and coated with 10 nm TiO_2 with addition of 150 nm CoO_x cocatalyst.

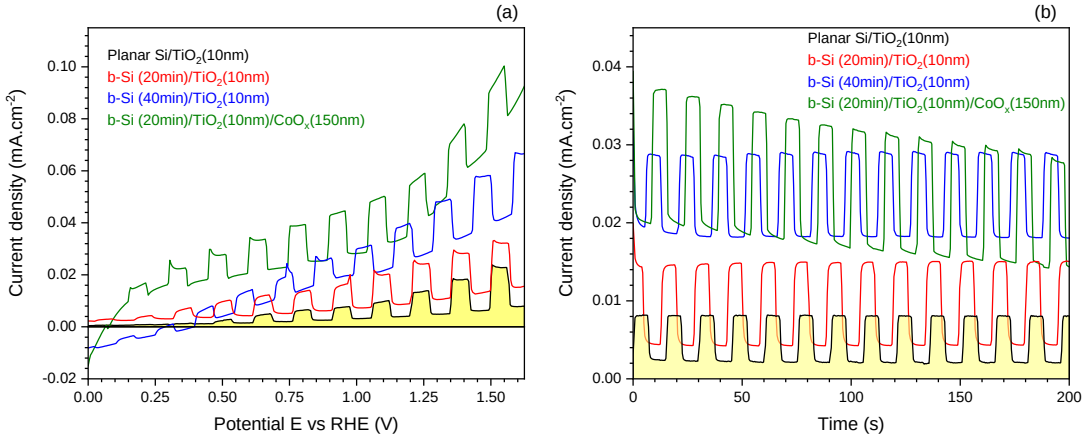

Figure 7. Potentiodynamic (a) and potentiostatic (b) scan at 1.23 V vs RHE for the Black-Si photoanodes fabricated for 20 and 40 min and coated with 10 nm TiO_2 with addition of 150 nm CoO_x cocatalyst layer in NaOH electrolyte under chopped light illumination. The potential scan speed was 10 mV/s and light ON-OFF chopping with ~ 8 s period in (a).

that fabrication conditions adopted in this study for the formation of heterostructured photoelectrode allowed to preserve the initial morphology of Black-Si substrate, contrary to the case reported in ref. [12], where top layer of $Co(OH)_2$ was electrodeposited on b-Si/TiO_2(8 nm) blocking large areas of underlying substrate underneath a thick coating.

The results of PEC investigations are summarized in Fig. 7 and compared with the response of planar Si photoelectrode with 10 nm TiO_2 coating as well as that of Black-Si fabricated for 40 min with 10 nm TiO_2. The increase in both dark- and photo-currents in the sequence: planar Si/TiO_2 (10 nm) < b-Si(20 min)/TiO_2(10 nm) < Black-Si(40 min)/TiO_2(10 nm) should be attributed to an increase in electrochemically active surface area of the electrode (Fig. 7(a)). It should be noted, however, that an increase in dark currents is more pronounced than that of photocurrents (taken as difference between the current values in dark and under illumination). Moreover, the increase in both dark- and photo-currents of planar-Si vs Black-Si is not comparable with increase in surface area of the samples (about 30 times) as discussed above. A possible explanation to this could be the mentioned energy barrier, which forms at the heterojunction between n-type Si and TiO_2 (Fig. 5). Deposition of CoO_x leads to significant increase in photocurrents, especially in the range of lower potential values, i.e. 0.1 V < E < 1.1 V. This can be attributed to efficient hole-mediated oxidation of water molecules to O_2 on the surface of cobalt oxide cocatalyst.

Chronoamperograms recorded under chopped illumination at the stationary potential of 1.23 V (Fig. 7(b)) reveal essentially the same trends as described above. A slight decay of PEC response of CoO_x-modified b-Si(20 min)/TiO_2(10 nm) sample can be observed during 200 s long measurement at

Preprints (www.preprints.org) | NOT PEER-REVIEWED | Posted: 10 April 2020 doi:10.20944/preprints202004.0169.v1

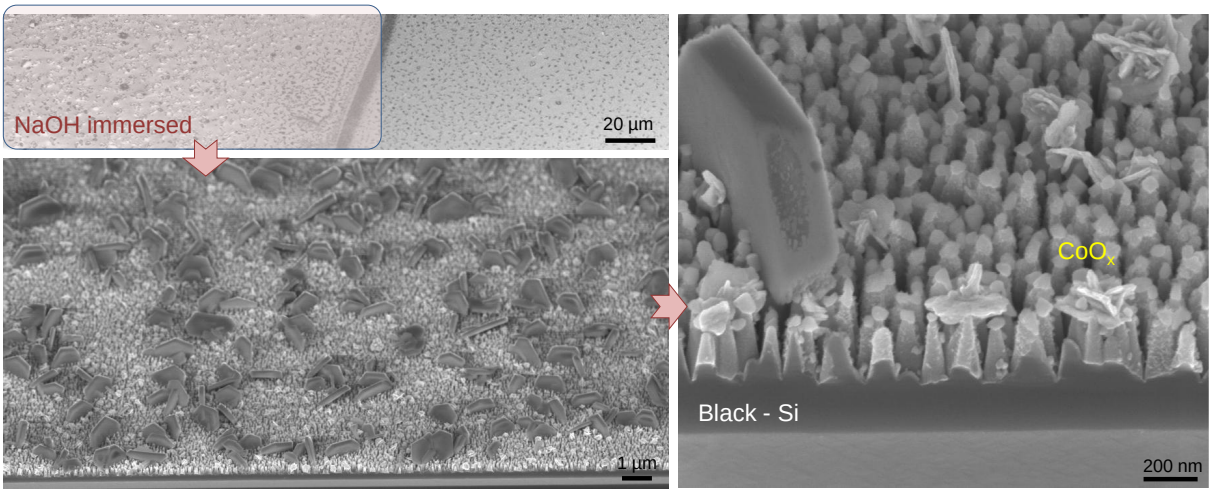

Figure 8. SEM images of Black-Si photoanodes etched for 20 min and coated with 10 nm TiO_2 with addition of 150 nm CoO_x cocatalyst after the exploitation for 30 min in photoelectrochemical cell.

1.23 V. This points to some rearrangement of the photoactive layer. SEM images of the photoelectrode made after the OER-exploitation in PEC cell for 30 min in NaOH electrolyte (Fig. 8) reveal drastic changes in the morphology of the sample with sub-micrometer sized hexagonal crystals randomly distributed all over the surface. Such morphology is characteristic to CoOOH [21], which is known to play the role of active site in oxygen evolution reaction [22].

The mechanism of photoelectrocatalytic OER on the surface of CoO_x-modified b-Si(20 min)/TiO_2(10 nm) could be as follows. Holes photogenerated in B-Si/TiO_2 drift to the electrode/solution interface, where they are captured by CoO_x. This interaction leads to oxidation of active cobalt oxide sites to Co(IV), the formation of which during photocatalytic water oxidation has been evidenced in ref. [23]. The authors suggested that two sequential hole injections convert the adjacent Co(III)–OH groups to Co(IV)=O centres. Subsequent addition of water molecule to one of the oxo sites leads to O-O bond formation, followed by reduction of both cobalt centres to Co(III) and catalyst recovery. Such catalytic oxidation/reduction cycle could explain recrystallization/restructuring of CoO_x layer seen in SEM images of the sample which underwent photoelectrochemical testing (Fig. 8). Irrespective of the rearrangement of cocatalyst layer during PEC performance, the spiky morphology of Black-Si is retained, which means that ALD-deposited conformal TiO_2 coating effectively protects silicon substrate from chemical dissolution in alkaline medium.

4. Conclusions and Outlook

Black-Si passivated with TiO_2 nano-layers deposited via ALD can be used as photo-anodes. Such surfaces can be utilised for deposition of co-catalyst of water oxidation to drive OER. Structural characterisation of photo-anodes based on Black-Si substrates show their nano-roughness which is instrumental for increase of surface area (current density) and reduction of reflectivity R (increase of absorbance $A = 1 - R - T$ where T is the transmittance). The experiments were carried out at 1.23 V potential, which is the thermodynamic potential of water oxidation to O_2, and could produce larger photo-currents at larger bias. This is particularly relevant for photo-electrolysis of water on TiO_2 [24] (Fig. 5) where strong increase in OER rate is observed at 1.77 V [25]. One further improvement of photo-anodes based on Black-Si could be achieved by removal of native SiO_2 on Si, which is ~ 2 nm and can be removed by Ar-plasma treatment. Native oxide is known to cause low photo-currents in photo-electrolysis of water and solar cells [25].

Black-Si coated with TiO_2 is also a promising biocidal (anti-viral and anti-bacterial) surface under UV light illumination with a strong oxidising (electron removal) property and can kill microbes on

 doi:10.20944/preprints202004.0169.v1

its surface. Conformal TiO_2 coating of 1-10 nm was not found to change the surface morphology of Black-Si (Fig. 2) and its bactericidal property is expected to be maintained [2] and augmented with photo-oxidation capability, demonstrated in this work. Furthermore, photo-oxidation capabilities can be also inferred from numerical simulations of light intensity distribution (Fig. A1). Surface coating of a nano-thin layer of TiO_2 or CoOx will cause a stronger absorbance inside the Black-Si needles due to to reduced reflectivity (Fig. A1). Thin surface layers can also contribute to a better charge separation and hole transport to the surface where oxidation of water (bacteria or virus) is taking place. Wurtzite CoOx is a p-type semiconductor with strong absorption of photons at 0.7-1.0 eV, which is considerably smaller than the direct bandgap energy of 1.6 eV [26]. A photo-anode with CoOx on Black-Si would harvest longer wavelengths at the surface while the positive bias of Black-Si contribute to e-h separation by electron extraction (see Fig. 5). A self-similar 3D fractal silicon fabrication with Hausdorff dimension of $D = 2.322$ was demonstrated using anisotropic etching of silicon [27] (see Appendix for the statistical and fractal definitions of AFM scans). Complex fractal 3D geometries with high porosity and surface area with conformal deposition by ALD are very promising for applications in light harvesting and photo-catalysis.

Author Contributions: Conceptualization, D.P.L., S.J., T.L.; experimentation, D.P.L., D.P., J.J., F.H., C.X.; data analysis, D.P.L., F.H., S.J., J.J.; investigation D.P.L., J.H., E.P.I., J.J.; data curation, D.P.L., S.J., J.J.; writing–original draft, D.P.L. and J.J.; writing–review and editing, all authors; project administration, D.P.L., T.L., S.J.

Funding: This research was funded by the ARC Discovery DP190103284 and JST CREST JPMJCR19I3 grants. We gratefully acknowledge support from the Swiss National Science Foundation (MARVEL NCCR and project 200021-159198).

Acknowledgments: Support of operational costs of Nanotechnology facility by Swinburne University of Technology 2016-19 is acknowledged. This work was performed in part at the Melbourne Centre for Nanofabrication (MCN) in the Victorian Node of the Australian National Fabrication Facility (ANFF).This work was supported in part by the AINSE ANSTO French Embassy (SAAFE) Research Internship Program.

Conflicts of Interest: The authors declare no conflict of interest.

Preprints (www.preprints.org) | NOT PEER-REVIEWED | Posted: 10 April 2020 doi:10.20944/preprints202004.0169.v1

Appendix

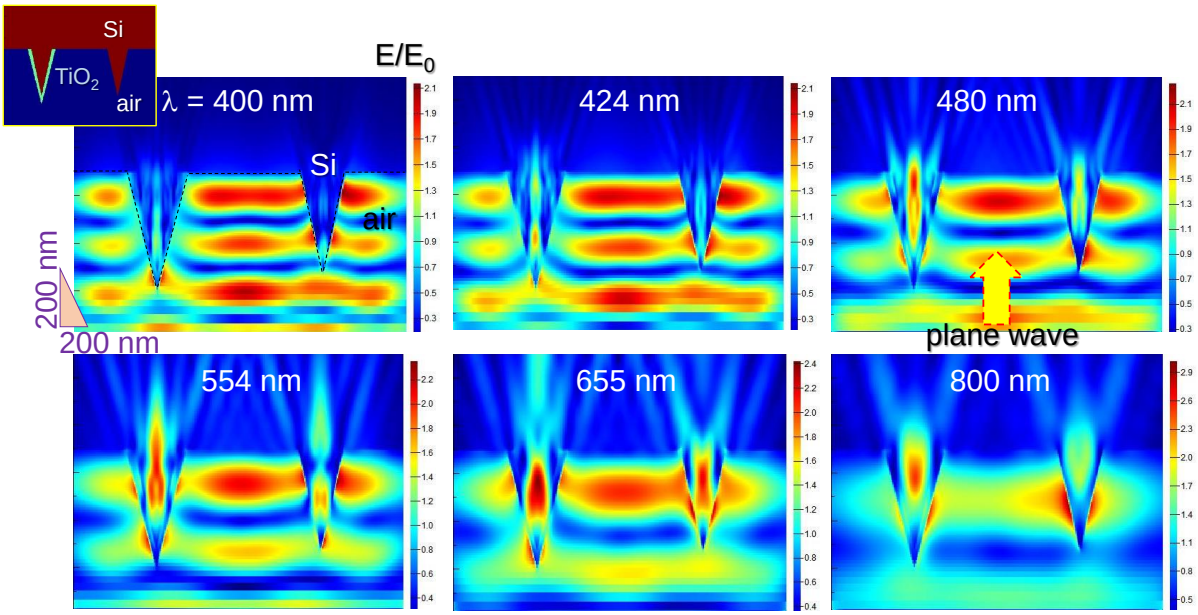

Figure A1. Finite differences time domain (FDTD) simulations (Lumerical) of light intensity distribution on Black-Si pyramids with 10 nm TiO_2 coating and without at different wavelengths λ. The inset shows the refractive index cross section where TiO_2 is modeled by $n = 2.5$ for all the wavelengths while refractive index of Si was taken from the Lumerical data base with real and imaginary parts $\tilde{n}(\lambda) = n(\lambda) + i\kappa(\lambda)$. The E-field is polarised in the plane of incidence and $E_0 = 1$.

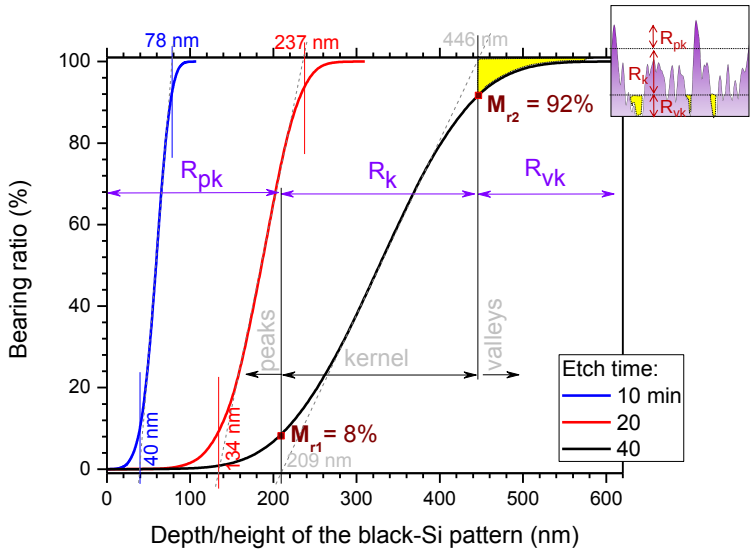

Figure A2. Bearing ratios of AFM traces (Fig. 1(b,c)) of b-Si etched for 10, 20 and 40 min. See text for definitions of the parameters marked on the the Firestone–Abbott bearing curve (standards DIN4776; STN ISO 13 565-2). Inset illustrates schematically the peak, kernel, and valley extent on actual AFM profile of 40 min etched Black-Si; yellow area-mark corresponds to the air pockets in the b-Si pattern which have height (depth) extent of R_{vk}.

Figure A1 shows exact numerical solution of Maxwell's equations for the plane wave incidence on b-Si pyramids. For comnparison one of the pyramids (left) is conformally covered by 10-nm-thick walls

Preprints (www.preprints.org) | NOT PEER-REVIEWED | Posted: 10 April 2020 doi:10.20944/preprints202004.0169.v1

of TiO_2. Even such a thin TiO_2 layer acts as an anti-reflection coating and creates higher light intensity E^2 inside Si nano-pyramid. The anti-reflection property of TiO_2 would be even more pronounced in water solution $n \approx 1.3$ at visible wavelengths as compared with air $n = 1$.

Figure A2 shows the Firestone–Abbott (F-A) bearing curves of b-Si etched for different times. The F-A curve is the cumulative probability density function of the surface profile's height which is calculated by integrating the profile of AFM trace. Each curve can be separated into the peak, kernel and valley sections after linear fit (tangential section) of the central part of the bearing ratio (see the marking for the 40 min etched sample). The positions of the minimum and maximum depth/height of the linear section of the AFM scan at intersections at bearing ratios of 0 and 100%, respectively, defines the kernel section (209 and 446 nm in Fig. A2). At those depth(height) values, the actual bearing ratios reads $M_{r1} = 8\%$ and $M_{r2} = 92\%$, which are are the mass ratios (DIN4776 standard). The area below the F-A curve up to the point M_{r1} represents the mass (an integral) of the most protruding peaks of surface roughness (the peaks region). The mass ratio point M_{r2} defines the point, which is excludes mass of the most deep valleys (the valleys region). The kernel roughness depth R_k is the thickness of the kernel at the flattest part of the bearing curve with the largest increase of material under the bearing curve. The reduced peak height R_{pk} and the reduced valley depth R_{vk} corresponds to the thickness of the bearing curve above (below) the central kernel profile, respectively. These parameters can be defined for surfaces etched for different times (Fig. A2) and lay foundation for statistical analysis of different surfaces.

The depth (height) profile is self-similar when roughness is investigated at different scales, hence is self-affine [28]. The Weierstrass-Mandelbrot (W-M) function is used for characterization of the height profile $z(x)$ along scan in x-direction. The W-M function has a fractal dimension, D [28]:

$$z(x) = G^{(D-1)} \sum_{n=n_l}^{\infty} \frac{\cos(2\pi\gamma^n x)}{\gamma^{n(2-D)}}; \; 1 < D < 2; \; \gamma > 1, \tag{A1}$$

where G is a scaling constant, $\gamma^n \equiv 1/\lambda_n$ is the frequency mode corresponding to the reciprocal of roughness wavelength λ_n; the low cut-off frequency is defined by the length L (AFM scan length here) as $\gamma^{n_l} = 1/L$. The fractal dimension $D = \frac{\log N}{\log m}$, where m is the magnification and N is the number of self-similar segments $1/m$, which form a line of unity length under magnification m ($(1/m) \times m = 1$); a one-dimensional linear segment is considered here as an example).

The fractal dimension D can be found from the power spectrum of $z(x)$, which is superimposed of infinite number of frequency modes and defines the amplitude of the roughness profile at different scales (AFM profile is considered here) [28]:

$$S(\omega) = \frac{G^{2(D-1)}}{2\ln\gamma} \cdot \frac{1}{\omega^{(5-2D)}}. \tag{A2}$$

If the power spectrum $S(\omega)$ is known, it is possible to calculate statistical parameters of the surface: the variances of the height, the slope and the curvature at different frequencies.

Another practical method to define the fractal dimension is based on the auto-correlation of AFM image (trace) [29]: $R(m, n)$ where m, n are integers describing a shift in x and y-directions, respectively, of the original image $z(x, y)$ which is made in N data acquisition steps. Then the structure function is defined as $S(m, n) = 2S_q^2(1 - R(m, n))$, where S_q is the root mean square roughness. Then the structure function of a self-similar pattern along the chosen direction τ follows $S(\tau) = K\tau^{2(2-D)}$ law [29], where K is the pseudo-topothesy (defines the absolute amplitude of spatial frequencies) and D is the fractal dimension. Nanoscale self-similar surface roughness from 20 nm to 300 nm (min-max height) was demonstrated on a thermally rescalled polystyrene coated with gold [30]. By changing scale of SEM images, self-similarity and fractal nature of such surfaces was evidenced.

The box-counting method applied to AFM or SEM images is one of the simplest ways to estimate fractal dimension [31]. The number of boxes $N(r) \propto r^{-D}$ of size r required to cover a chosen feature in

the image provides direct estimate of the fractal dimension D from the slope when log-log plot is made $N(r)$ vs. r. A systematic structure analysis by bearing ratio and fractal dimension of nanostructures is urgently required for understanding their link with biocidal (anti-viral and antibacterial) properties of such surfaces, e.g. b-Si [2].

References

1. Jansen, H.; de Boer, M.; Legtenberg, R.; Elwenspoek, M. The black silicon method: a universal method for determining the parameter setting of a fluorine-based reactive ion etcher in deep silicon trench etching with profile control. *Journal of Micromechanics and Microengineering* **1995**, *5*, 115. doi:10.1088/0960-1317/5/2/015.
2. Ivanova, E.P.; Hasan, J.; Webb, H.K.; Gervinskas, G.; Juodkazis, S.; Truong, V.K.; Wu, A.H.F.; Lamb, R.N.; Baulin, V.; Watson, G.S.; Watson, J.A.; Mainwaring, D.E.; Crawford, R.J. Bactericidal activity of nanostructured black silicon. *Nature Commun.* **2013**, *4*, 2838.
3. Pham, V.T.H.; Truong, V.K.; Mainwaring, D.; Guo, Y.; Baulin, V.; Kobaisi, M.A.; Gervinskas, G.; Juodkazis, S.; Zeng, W.R.; Doran, P.; Crawford, R.J.; Ivanova, E.P. Nanotopography as a trigger for the microscale, autogenous and passive lysis of erythrocytes. *J. Mater. Chem. B* **2014**, *2*, 2819 – 2826.
4. Langer, C.; Prommesberger, C.; Ławrowski, R.; Schreiner, R.; Serbun, P.; Müller, G.; Düsberg, F.; Hofmann, M.; Bachmann, M.; Pahlke, A. Field emission properties of p-type black silicon on pillar structures. *J. Vacuum Sci. Technol. B* **2020**, *34*, 02G107.
5. Seniutinas, G.; Gervinskas, G.; Verma, R.; Gupta, B.D.; Lapierre, F.; Stoddart, P.R.; Clark, F.; McArthur, S.L.; Juodkazis, S. Versatile SERS sensing based on black silicon. *Optics Express* **2015**, *23*, 6763 – 6772.
6. Ščajev, P.; Malinauskas, T.; Seniutinas, G.; Arnold, M.D.; Gentle, A.; Aharonovich, I.; Gervinskas, G.; Michaux, P.; Hartley, J.S.; Mayes, E.L.H.; Stoddart, P.R.; Juodkazis, S. Light-induced reflectivity transients in black-Si nanoneedles. *Solar Energy Mater. Solar Cells* **2016**, *144*, 221–227.
7. Nishijima, Y.; Komatsu, R.; Ota, S.; Seniutinas, G.; Balčytis, A.; Juodkazis, S. Anti-reflective surfaces: Cascading nano/microstructuring. *Appl. Phys. Lett.: Photonics* **2016**, *1*, 076104.
8. Shoji, T.; Mototsuji, A.; Balcytis, A.; Linklater, D.; Juodkazis, S.; Tsuboi, Y. Optical tweezing and binding at high irradiation powers on black-Si. *Sci. Reports* **2017**, *7*, 12298.
9. Pekarek, R.T.; Christensen, S.T.; Liu, J.; Neale, N.R. Energetic Effects of Hybrid Organic/Inorganic Interfacial Architecture on Nanoporous Black Silicon Photoelectrodes. *Sustainable Energy and Fuels* **2019**, *3*, 1600–1667.
10. Yang, F.; Aguiar, J.A.; Fairchild, M.; Vakki, W.; Younan, S.; Zhou, Y.; Zhuo, L.; Gu, J. Dual Protection Layer Strategy to Increase Photoelectrode–Catalyst Interfacial Stability: A Case Study on Black Silicon Photoelectrodes. *Adv. Mater. Interfaces* **2019**, p. 1802085.
11. Oh, K.; Joanny, L.; Gouttefangeas, F.; Fabre, B.; Dorcet, V.; Lassalle-Kaiser, B.; Vacher, A.; Meriadec, C.; Ababou-Girard, S.; Loget, G. Black Silicon Photoanodes Entirely Prepared with Abundant Materials by Low-Cost Wet Methods. *ACS Appl. Energy Mater.* **2019**, *2*, 1006–1010.
12. Yu, Y.; Zhang, Z.; Yin, X.; Kvit, A.; Liao, Q.; Kang, Z.; Yan, X.; Zhang, Y.; Wang, X. Enhanced photoelectrochemical efficiency and stability using a conformal TiO2 film on a black silicon photoanode. *Nature Energy* **2017**, *2*, 17045.
13. Yao, X.; Schneider, C.W.; Lippert, T.; Wokaun, A. Manipulation of ion energies in pulsed laser deposition to improve film growth. *Appl. Phys. A* **2019**, *125*, 344.
14. Gervinskas, G.; Seniutinas, G.; Hartley, J.S.; Kandasamy, S.; Stoddart, P.R.; Fahim, N.F.; Juodkazis, S. Surface-enhanced Raman scattering sensing on black silicon. *Annalen der Physik* **2013**, *525*, 907–914.
15. Balčytis, A.; Ryu, M.; Seniutinas, G.; Nishijima, Y.; Hikima, Y.; and, M.Z. Si-based infrared optical filters. *Opt. Eng.* **2015**, *54*, 127103 – 127103.
16. Buividas, R.; Fahim, N.; Juodkazytė, J.; Juodkazis, S. Novel method to determine the actual surface area of a laser-nanotextured sensor. *Appl. Phys. A* **2013**, *14*, 169–175.
17. Juodkazis, K.; Juodkazytė, J.; Šebeka, B.; Savickaja, I.; Juodkazis, S. Photoelectrochemistry of silicon in HF solution. *J. Solid State Electrochem.* **2013**, *17*, 2269–2276.
18. Brack.; Dann, S.E.; Wijayantha, K.; Adcock, P.; Foster, S. An assessment of the viability of hydrogen generation from the reaction of silicon powder and sodium hydroxide solution for portable applications. *Int. J. Energy Res.* **2017**, *41*, 220–228.

19. Mizeikis, V.; Kowalska, E.; Juodkazis, S. Resonant localization, enhancement, and polarization. In *Nanoplasmonics: Advanced Device Applications*; J W M Chon.; Iniewski, K., Eds.; CRC Press, 2009; p. 126–134.
20. Si, W.; Pergolesi, D.; Haydous, F.; Fluri, A.; Wokaun, A.; Lippert, T. Investigating the behavior of various cocatalysts on $LaTaON_2$ photoanode for visible light water splitting. *Phys. Chem. Chem. Phys.* **2017**, *19*, 656–662.
21. Yang, J.; Liu, H.; Martens, W.N.; Frost, R.L. Synthesis and Characterization of Cobalt Hydroxide, Cobalt Oxyhydroxide, and Cobalt Oxide Nanodiscs. *J. Phys. Chem. C* **2010**, *114*, 111–119.
22. Stevens, M.; Kast, M.; Trotochaud, L.; Smith, A.; Boettcher, S. Cobalt–Iron (Oxy)hydroxide Oxygen Evolution Electrocatalysts: The Role of Structure and Composition on Activity, Stability, and Mechanism. *J. Am. Chem. Soc.* **2015**, *137*, 10.1021/jacs.5b00281.
23. Zhang, M.; de Respinis, M.; Frei, H. Time-resolved observations of water oxidation intermediates on a cobalt oxide nanoparticle catalyst. *Nature Chem* **2014**, *6*, 362–367.
24. Juodkazis, K.; Juodkazytė, J.; Kalinauskas, P.; Jelmakas, E.; Juodkazis, S. Photoelectrolysis of Water: Solar Hydrogen - Achievements and Perspectives. *Opt. Express: energy express* **2010**, *18*, A147–A160.
25. Juodkazytė, J.; Seniutinas, G.; Šebeka, B.; Savickaja, I.; Malinauskas, T.; Badokas, K.; Juodkazis, K.; Juodkazis, S. Solar water splitting: efficiency discussion. *Int. J. Hydrogen Energy* **2016**, *41*, 11941 – 11948.
26. Wang, Y.; Ge, H.X.; Chen, Y.P.; Meng, X.Y.; Ghanbaja, J.; Horwat, D.; Pierson, J.F. Wurtzite CoO: a direct band gap oxide suitable for a photovoltaic absorber. *Chem. Commun.* **2018**, *54*, 13949–13952.
27. Berenschot, E.; Jansen, H.V.; Tas, N.R. Fabrication of 3D fractal structures using nanoscale anisotropic etching of single crystalline silicon. *J. Micromech. Microeng.* **2013**, *23*, 055024.
28. Majumdar, A.; Bhushan, B. Role of Fractal Geometry in Roughness Characterization and Contact Mechanics of Surfaces. *J. Tribol.* **1990**, *112*, 205 – 216.
29. Ş Ţalu.; Bramowicz, M.; Kulesza, S.; Pignatelli, F.; Salerno, M. Surface Morphology Analysis of Composite Thin Films based on Titanium-Dioxide Nanoparticles. *Acta Physica Polonica* **2017**, *131*, 1529–1533.
30. Balcytis, A.; Ryu, M.; Seniutinas, G.; Stoddart, P.R.; Mamun, M.; Morikawa, J.; Juodkazis, S. Nano-rescaling of gold films on polystyrene: thermal management for SERS. *Nanoscale* **2017**, *9*, 690–695.
31. Nonomura, Y.; Seino, E.; Abe, S.; Mayama, H. Preparation and Characterization of Fractal Elastomer Surfaces. *J. Oleo Sci.* **2013**, *62*, 587–590.